7

Fluorinated SnO_2 for VOCs Detection

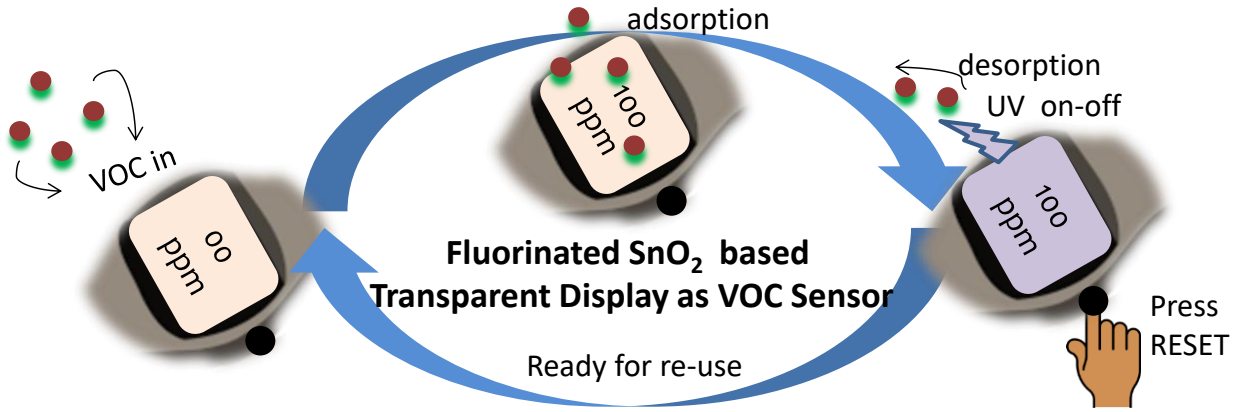

7.1 Introduction

Healthcare and environmental sensors has been given immense attention because of ever-increasing pollutants including VOCs. Almost every human activity including cooking, driving, industrial operation, air conditioning, etc. releases harmful organics to the environment. While the outdoor environment may have regulations regarding exposure limits, the indoor environment is often unregulated and VOCs often appear in greater concentrations in the indoor environment. VOC sensors with lower limit of detection (LOD) is explored for non-invasive disease diagnostics by analyzing VOC content in human breath. The commonly used portable instruments for VOC detection are the hand-held photo-ionization detectors, making it bulky and costly solution. Tin oxide (SnO_2) based chemiresistive VOC sensors have ruled the sensor market since 1960s due to easy productivity, low cost and good portability. Despite of the various efforts in the literature, VOC sensors still suffer drawbacks of high working temperature and non specificity towards analytes. Apart from the specificity towards chemical analytes, the sensors also respond towards various fluctuations like pressure, temperature, humidity, particulate matter and thus reducing the reliability of the sensor In the literature, amidst all the approaches for modification of SnO_2, it is observed that the fluorine-doped tin oxide (FTO) has been put aside in the context of application in VOC sensing. However, FTO is a wide bandgap (~3.6 eV) degenerate semiconductor with exceptional electrical, optical and chemical properties, and has been extensively used as transparent and conducting substrate for a variety of applications in transparent electronics [Liu et al., 2010; Singkammo et al., 2015]. SnO_2 is doped with fluorine to a level of ~5-10% by physical methods to increase its conductivity without compromising significantly on optical transmittance [Dixon et al., 2016]. Fluorine being a small size atom, can diffuse in the oxygen vacancy as well as interstitial sites of the stable tin oxide and modify the electronic properties from semiconducting to highly conducting [Banyamin et al., 2014; Dixon et al., 2016; Wang et al., 2017e]. Thus, controlling the extent of fluorination and the nature of fluorination is critical. If the fluorination of SnO_2 be limited to the surface by tuning the degree of fluorination, one can possibly enhance the VOC sensing performance due to chemical activation and modulation of its electronic structure [Suffner et al., 2010].

7.1.1 Objectives of Work

Incorporation of fluorine into metal oxide nanomaterials can tune their chemical and physical properties and effect the sensing performance by influencing the oxygen vacancies and oxygen adsorption at the sensor, key phenomena for metal oxide based sensors. The objectives of this work are as follows:
1: Optimization and control of fluorination to low percentages (<1%) for a significant response of F-SnO_2 towards VOC exposure at low temperatures.
2: To reduce the persistent photoconductivity (PPC) effect observed in SnO_2.
3: To test an innovative photochemiresistive approach of UV on-off for sensor recovery at lower operating temperatures.

7.2 Experimental

7.2.1 Fabrication of Pristine and Fluorinated SnO_2 Film

A SnO_2 precursor solution (1 M) was prepared by dissolving 3.38 g $SnCl_2.2H_2O$ in 15 mL ethanol and then stirring at room temperature for 6 hours for aging. 0.6 mL of the as-prepared solution was spin-coated on a 2.5×2.5 cm^2 glass substrate at a speed of 1000 rpm for 60 s. The film was then annealed on a hotplate pre-heated at 500 °C for 15 min to form a smooth film of SnO_2. For fluorination of the freshly prepared film, it was placed in 0.01 M Selectfluor (Chloromethyl-4-fluoro-1,4-diazoniabicyclo[2.2.2]octane bis(tetrafluoroborate)) solution in acetonitrile at 60 °C for 1 h for low-doping, which was followed by washing with acetonitrile and heating at 150 °C for 15 min. For heavily-doped films, a 0.1 M solution was used.

7.2.2 Characterization

XRD (D8, Bruker) with Cu Kα radiation (λ= 1.5418 Å) has been carried out to investigate the structural properties of the films before and after fluorination. FESEM imaging (Nova NanSEM 600) has been performed to analyze the surface morphology of the films. UV-visible spectroscopy (Varian Cary 4000) measurements have been performed to get the transmittance in the range of 200-800 nm. Film thickness was measured by Stylus Profilometer (Bruker, Dektak-T). XPS measurements were performed on the Thermo-scientific NEXSA surface analysis system.

7.2.3 Low-temperature Conductivity Measurements

The glass substrates coated with pristine or fluorinated SnO_2 film were cut into 2.5 × 1 cm^2 pieces, and then Ag paint contacts were taken to maintain the sensing area of 1 × 0.5 cm^2. Low-temperature conductivity measurements were performed up to liquid nitrogen temperature using the CH-660 electrochemical workstation by applying a bias voltage of 1 V to the devices while placing on a Linkam stage (THMS Linkam Scientific THMS 600) having precise temperature control (up to 0.1°C).

7.2.4 Fabrication of Al Mesh Heater

The aluminum mesh heater was prepared by crack network templating method reported in the literature [Gupta et al., 2014, 2016b, 2017; Rao et al., 2014]. The colloidal dispersion of acrylic resin nanoparticles (CP) (1/1; v/v) was sprayed on the backside of the glass substrate with SnO_2 films and left for drying at room conditions (5 min). After cracking, the well-interconnected crack which is down to the substrate was used as a template to deposit Al metal, using a vacuum deposition technique (Hind Hivac, India). Finally, the CP film was washed using chloroform, leaving the interconnected Al network wire network on the glass substrate. The pristine and F-SnO_2 films were coated only after the Al network fabrication process. The silver paste was brushed on opposite edges of the film as contacts. The substrate is heated by Joule heating, and imaging is done from the backside of the Al metal network.

7.2.5 Temperature Measurements

Self-regulated DC voltage was supplied to the metal network-based heater through a source-meter. Thermal imaging was carried out in the open environment using a thermal imaging camera (Testo 885-2). Temperature versus power per unit area plot is derived from the data obtained and used for approximating the temperature of the sensor surface inside the gas sensing chamber. The temperature of the commercial MQ3 sensor is also measured by thermal imaging.

7.2.6 Photoconductivity Measurements

Ag paint was coated across the width over either side of the glass substrate keeping an active sensing area of 0.5 cm^2 in the middle of the SnO_2 film. The photoconductivity measurements were performed using the CH-660 electrochemical workstation by applying a bias voltage of 1 V to the devices while heating was controlled by regulating the voltage input on the integrated Al mesh heater. The films were illuminated with a type-A UV LED (365 nm) source with an intensity of 1 mA/cm^2. The photoresponse (R) is calculated using the formula : $R = (R_t - R_o)/R_o \times 100$, where R_t is resistance at any time, t and R_o is the resistance at t=0. The decay time for each profile is measured as the time taken for a 90% drop in the photoresponse upon turning-off the UV illumination.

7.2.7 Gas Sensing Measurements

The photoconductivity measurement setup was kept in a controlled environment gas chamber through which VOCs were passed at a constant flow rate for the sensing measurements. Non-steady state VOCs were generated in a hot RB flask of 2 L under constant nitrogen flow (12 bubbles/s) conditions. Gas temperature was measured to be around 55-60 °C, and the gas concentration was estimated to be ~760 ppm using calibration data of the commercial MQ3 sensor [https://datasheetspdf.com/pdf-file/904630/ETC/MQ303A/1, n.d.]. The outlet of the VOC was connected with the inlet gas chamber with the tubing. I-t characteristics in presence or absence of VOCs were measured on CH-660 electrochemical at a bias voltage of 1 V. At a particular concentration of VOC, the measurement was performed until all the VOC was flushed out by the carrier gas at the same flow rate and the device came back to its initial state. Steady-state gas sensing at low concentrations was performed in a custom-designed setup. A fixed concentration of VOC was prepared in a mixer chamber using zero air as diluting and carrier gas. The known concentrations of VOC are injected into the sensing chamber at a flow rate of 2000 sccm using mass flow controllers (Alicat).

7.3 Result and Discussion

7.3.1 Concept of Work

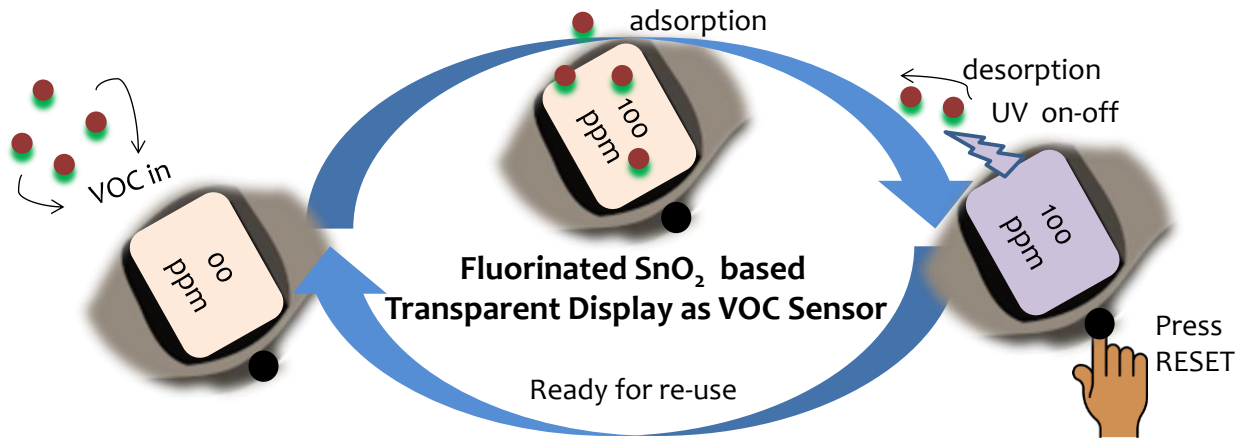

Figure 7.1 Schematic showing the working of F-SnO_2 based transparent display as VOC sensor.

Commercial volatile organic compound (VOC) sensors are mainly based on bulk SnO_2 semiconducting films, which, however, require high temperatures (~ 350 °C) for optimal operation [Das et al., 2014; Lin et al., 2019]. While such requirement is presently met with using a supplementary heater, a design principle that can make the device work at near ambient temperatures would be a technological milestone. The issue at hand is the sluggish recovery behavior of the SnO_2 film past its exposure to the VOCs. Surface activation of SnO_2 and hybrids by UV exposure during VOC response can bring down the operating temperature. However, the continuous exposure to UV during long detection hours due to slow recovery can not only be power consuming but also very harmful for an application where the sensor itself is a transparent display. In this study, a transparent display-based VOC sensor is proposed as demonstrated in Figure 7.1.

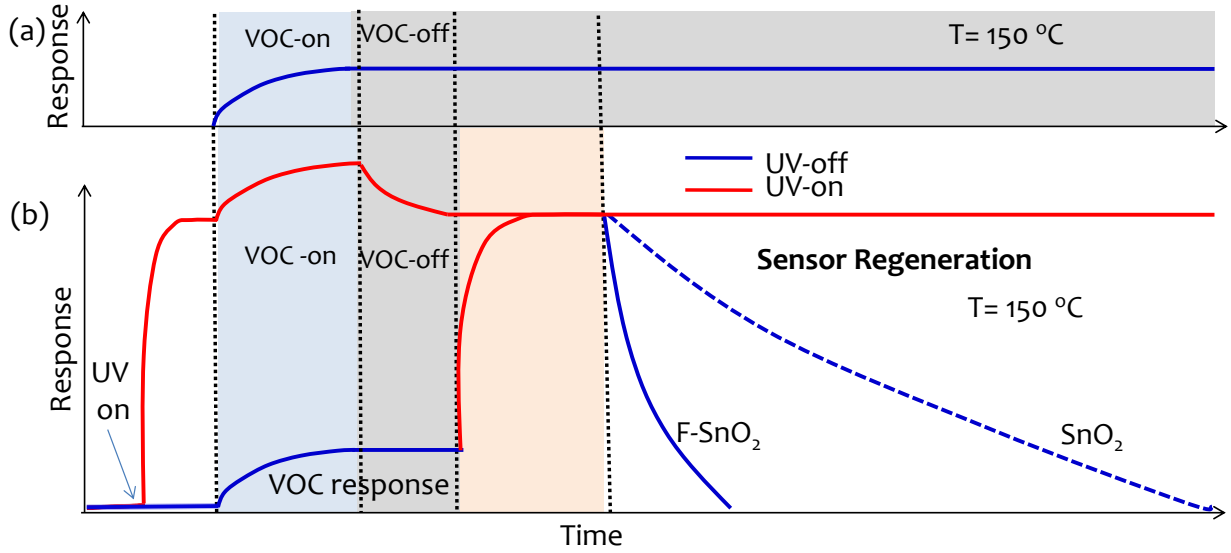

Figure 7.2: Hypothetical data demonstrating (a) typical response of a VOC sensor at low temperature (150 °C) with no recovery for prolonged hours, (b) sensor recovery process on activation by UV-illumination for pristine SnO_2 and F-SnO_2-based sensor at an operating temperature of 150 °C after exposure to VOCs.

A transparent semiconducting film based VOC sensor is designed that recovers by a "sensor reset" process once a saturated VOC response is obtained. A short UV pulse is sufficient enough to recover the sensor from a typical hangover-type behavior of sensing element after VOC exposure (Figure 7.2a). However, in the case of SnO_2, UV pulse results in persistent photoconductivity (PPC) effect from slow recombination of the photo-induced charge carriers, and that offsets the advantage of UV usage in such a sensor design [Liu et al., 2015a; Morais et al., 2007; Tierney et al., 2016; Viana et al., 2013]. Thus, we have fabricated fluorinated SnO_2 (F-SnO_2) films with reduced PPC effect. Once the signal from any of the VOC is obtained, the UV is turned on-off for desorption of chemisorbed organic molecules, and with fluorinated SnO_2, photoresponse decays quickly to the baseline value at 150 °C itself which otherwise does not recover on its own even after several hours due to PPC effect in SnO_2 (Figure 7.2b).
On the contrary, if the UV light is continuously kept on, the baseline of the sensor will be expected to shift to higher values due to contributions from the photo-induced current, as shown schematically by the red curve in Figure 7.2b. The decay of gas sensor response to baseline value will be relatively quick in UV light due to the desorption of chemisorbed organic molecules. Nevertheless, continuous UV-on condition may not be practically safe for a transparent display sensor proposed in this study.

7.3.2 Gas Sensing Mechanism

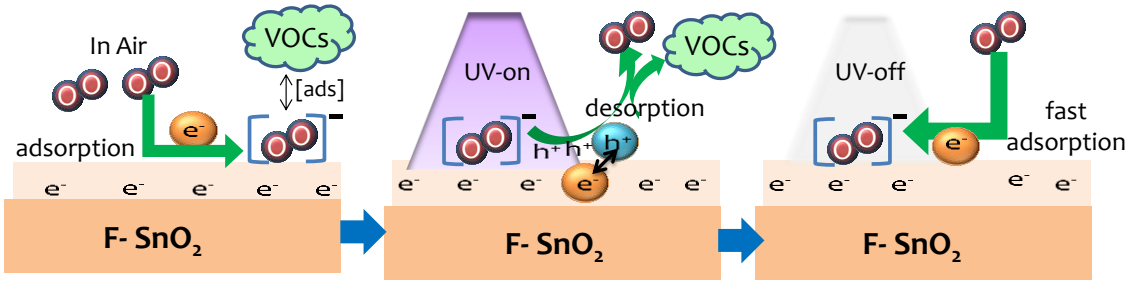

Figure 7.3: Schematic showing mechanism behind the working of F-SnO_2 based VOC sensor.

Mechanistically, in case of pristine and F-SnO_2 (n-type semiconductor), oxygen in air captures the free electrons and gets adsorbed on semiconductor surface, forming negatively charged species. When the UV light is turned-on, photo-excited holes compensate the charged oxygen ions that get desorbed from the surface as oxygen molecules leaving behind photo-excited electrons on the surface. However, on turning-off the UV, the F-SnO_2 due to relatively more number of free electrons than SnO_2 again participates in oxygen molecule adsorption at a much faster rate resulting in a faster decay of persistent photocurrent. Parallelly, the oxygen ions adsorbed on the surface react with the VOC molecules and gives a significant response that decays again on exposure to a UV pulse (Figure 7.3). This concept is elaborated with experimental observations in this chapter.

7.3.3: Optimization of Fluorination

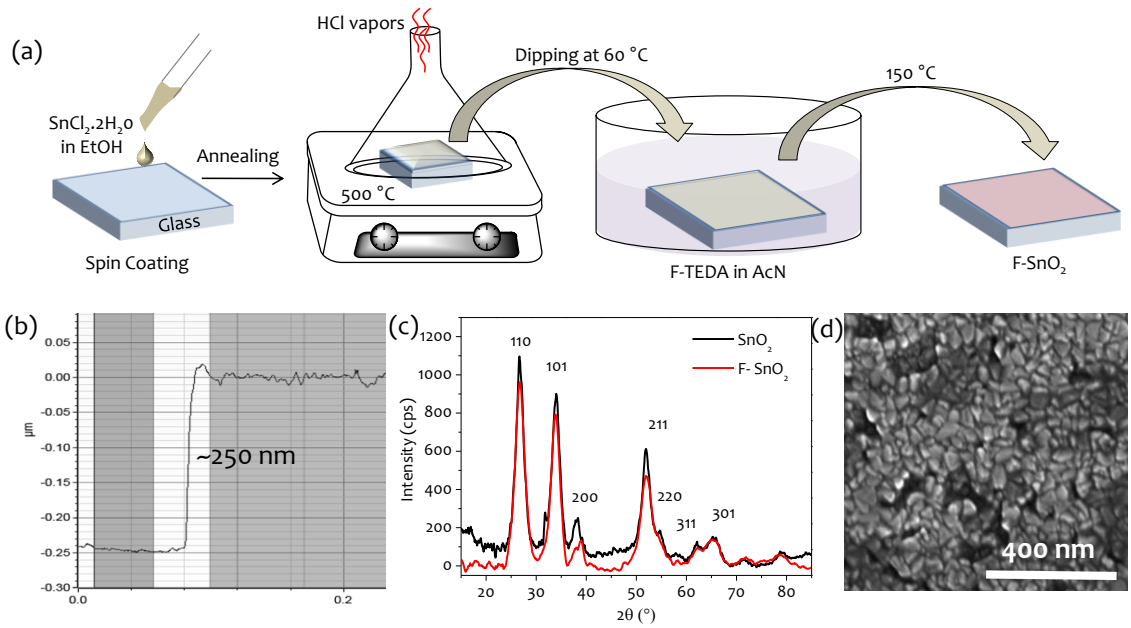

Figure 7.4: (a) Schematic demonstration of the fabrication process of F-SnO_2 films. (b) SnO_2 film thickness measurement using surface profilometer. (c) XRD patterns of SnO_2 and F-SnO_2 and (d) FESEM image of F-SnO_2 film.

Figure 7.4a describes the experimental procedure involved in the fabrication of F-SnO_2 film. Briefly, a 250 nm thick SnO_2 film (Figure 7.4b) was fabricated by spin coating of hydrous $SnCl_2$ solution in ethanol on glass substrates followed by annealing on a pre-heated hotplate at 500 °C for 15 min. In the second step, fluorination was performed by dipping SnO_2 film in an electrophilic fluorinating agent, Selectfluor™ (F-TEDA) solution. Among common fluorinating agents, Selectfluor™ is extremely safe to handle that decomposes and gradually release electrophilic fluorine species at relatively low temperatures that react with the SnO_2 surface. The fluorination process and conditions (time, concentration, and temperature) were optimized, and experimental details are tabulated in Table 7.1. The amount and nature of doping (substitutional/interstitial) are tuned by modulating the concentration of the fluorinating precursor. The crystal structure of the SnO_2 films was analyzed before and after fluorination.

The SnO_2 XRD data (Figure 7.4c) shows the rutile structure of SnO_2 that is unaltered on fluorination, while the FESEM image shows a uniform coating of polygonal nanoparticles for F-SnO_2 film (size ~40-50 nm, Figure 7.4d).

Table 7.1: Optimization of conditions for SnO_2 fluorination.

	Treatment process	Time (h)	Conc. (M)	Temp. (°C)	Transparency	Observation
1	Dipping in F-TEDA	24	0.1	RT	-	SnO_2 film peeled off
2	Drop-casting F-TEDA on SnO_2	-	0.05	60	Transparent	No change
3	Drop-casting F-TEDA on SnO_2	-	0.05	150	Film turned black	>1 order decrease in resistivity
4	Drop-casting F-TEDA on SnO_2	-	0.05	200	Film turned black	>1 order decrease in resistivity
5	Dipping in F-TEDA followed by heating at 150 °C	10 min	0.2	80	-	SnO_2 film peeled off
6	Dipping in F-TEDA followed by heating at 150 °C	1	0.1	80	-	SnO_2 film peeled off
7	Dipping in F-TEDA followed by heating at 150°C	1	0.1	70	-	SnO_2 film peeled off
8	Dipping in F-TEDA followed by heating at 150°C	1.5	0.1	60	-	SnO_2 film peeled off
9	**Dipping in Selectfluor™ followed by heating at 150 °C**	**1**	**0.01**	**60**	**Transparent**	**>1 order decrease in resistivity (low fluorine doping 0.6 at %, substitutional doping)**
10	Dipping in F-TEDA followed by heating at 150°C	1	0.1	60	Transparent	Slight change in resistivity (high fluorine doping ~5.7 at%, substitutional and interstitial doping)

7.3.4 XPS of F-SnO_2

The presence of fluorine can be ascertained based on the F1s core-level spectrum, which shows a small but distinct peak at 684.7eV, amounting to ~ 0.6 at.% of fluorine substituting oxygen vacancies in the SnO_2 lattice (Figure 7.5a). The high-resolution Sn spectra of F-SnO_2 and SnO_2 show the presence of Sn $3d_{5/2}$ and $3d_{3/2}$ peaks at ~486.58 eV and ~ 494.98 eV, respectively, with insignificant change upon fluorination (Figure 7.5b). SnO_2 and F-SnO_2 exhibit O1s peak with atomic oxygen percentages of 40.1% and 35.8%, respectively. The O1s peak can be further deconvoluted into three peaks, as shown in Figure 7.5c,d. The first peak at ~530 eV corresponds to the O-Sn^{4+} species forming [SnO_6] octahedrons, the second peak (~531 eV) is related to O-Sn^{2+} due to non-stoichiometric oxygen defects, and third peak (~533 eV) appears due to chemisorbed oxygen species (O_{chem}).

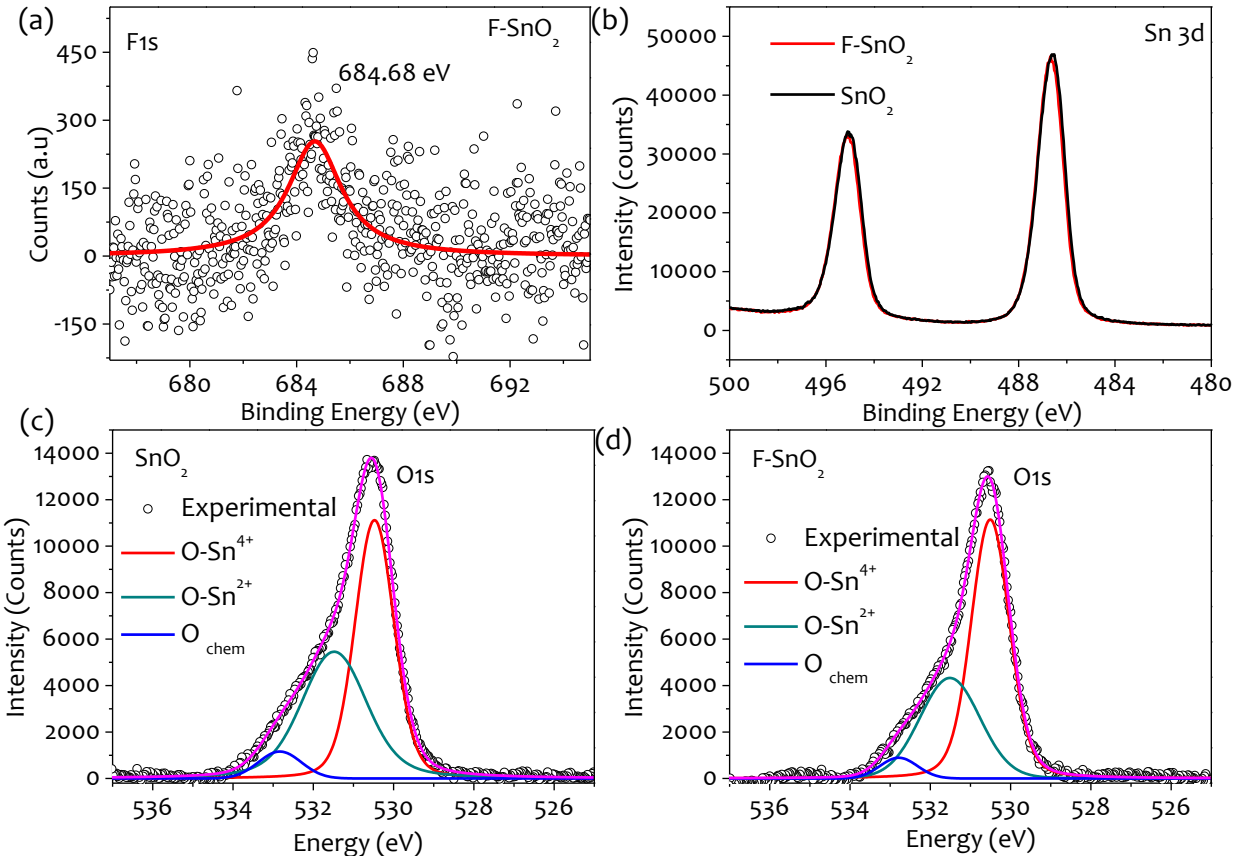

Figure 7.5: (a) High-resolution F1s XPS spectrum of F-SnO_2 (b) Comparative high-resolution Sn3d XPS spectra of SnO_2 and F-SnO_2. (c,d) Deconvoluted O1s XPS spectra of SnO_2 and F-SnO_2, respectively.

The peak positions and corresponding area under the curve are shown in Table 7.1. SnO_2 exhibits O-Sn^{2+}/ O-Sn^{4+} ratio of 0.85 which decreases to 0.57 upon fluorination (Table 7.3). The atomic percentages of oxygen defects in SnO_2 and F-SnO_2 are calculated to be 17.2% and 12.1%, respectively (Table 7.3).

Table 7.2: XPS analysis of O1s for SnO_2 and F-SnO_2 films.

	O-Sn^{4+}		**O-Sn^{2+}**		**Ratio**	**O_{Chem}**		**Oxygen defect ratio**
Sample	Peak (eV)	Area under the curve	Peak (eV)	Area under the curve	O-Sn^{2+}/ O-Sn^{4+}	Peak (eV)	Area under the curve	O-Sn^{2+}/ (O-Sn^{2+}+O-Sn^{4+}+O_{Chem})
SnO_2	530.47	14638.1	531.48	12528.1	0.85	532.83	1548.2	0.43
F-SnO_2	530.51	14549.4	531.51	8303.4	0.57	532.79	1042.2	0.34

Table 7.3: Percentage of oxygen defects (%) in SnO_2 and F-SnO_2.

	Total O1s (%)	Oxygen defect ratio	% oxygen defect
SnO_2	40.1	0.43	17.24
F-SnO_2	35.8	0.34	12.17

7.3.5 F-SnO_2: Optical and Electrical Characteristics

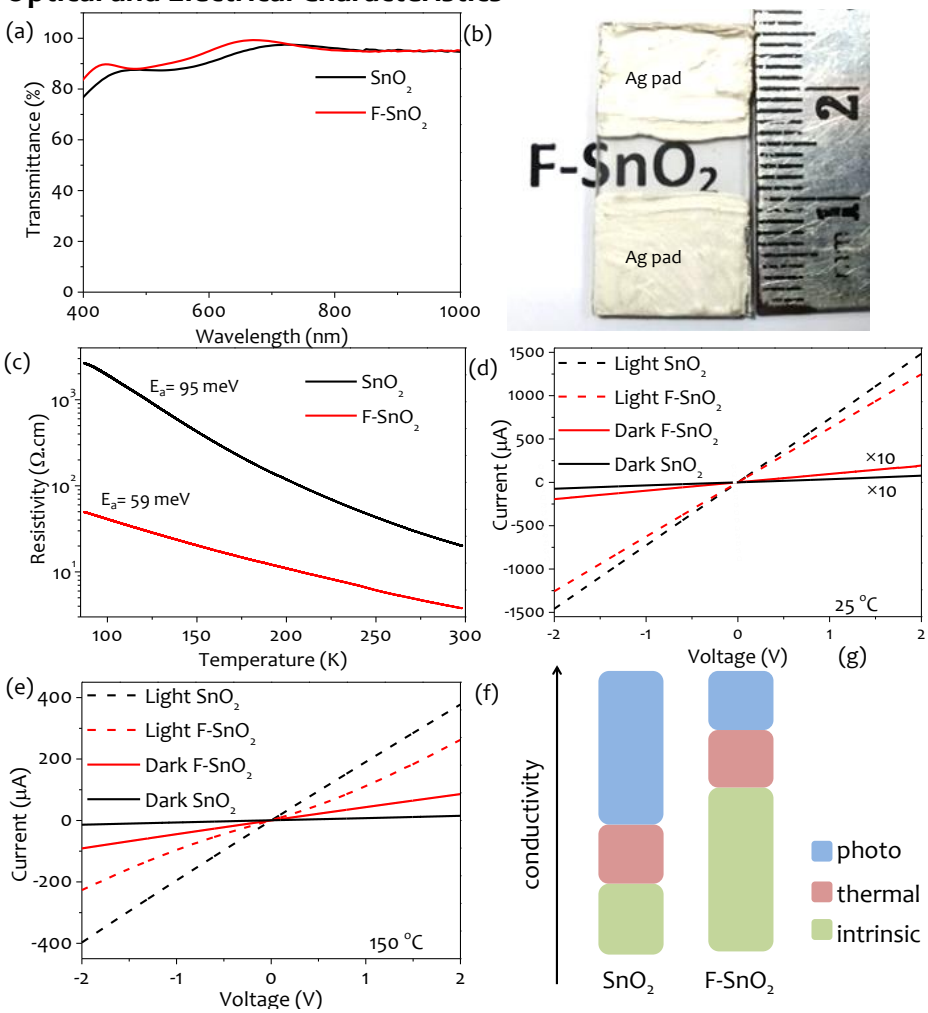

Figure 7.6: (a) Optical transmittance of SnO_2 and F-SnO_2 films. (b) Photograph of the transparent F-SnO_2 sensor. (c) Low-temperature resistivity plot for SnO_2 and F-SnO_2 films. I-V characteristics of the films in the dark and under UV-illumination of 365 nm wavelength at (d) 25°C and (e) 150°C, respectively. (f) Contributions to the inherent conductivity of SnO_2 and F-SnO_2 from thermal and photo-induced carriers (y-axis is not to the scale; it is a conceptual depiction for clarity).

Figure 7.6a shows that the difference in transmittance of the pristine and fluorinated SnO_2 (0.6 at%, expressed as F-SnO_2 unless specified) is almost insignificant in the entire visible region of the electromagnetic spectrum. Ag paint contacts were formed on either side of the F-SnO_2 film with 0.5 cm^2 exposed film area for further measurements as shown in Figure 7.6b. Low-temperature resistivity measurements (Figure 7.6c) show that the pristine film exhibits a semiconducting behavior with three orders change in resistivity upon cooling down to 87 K similar to literature results [Geraldo et al., 2003]. Interestingly, the resistivity of F-SnO_2 at room temperature is lower by an order in comparison to that of the pristine film, ~ 3.7 and ~ 20 Ω.cm, respectively. The doped film showed just above an order increase in resistivity upon cooling (~ 49 Ω.cm at 87 K, see Figure 7.6c). The conduction process in the films can be examined from temperature-dependent resistivity in the higher temperature range (200-300 K) using Arrhenius equation as [Lin et al., 2014]:

$$\sigma(T) = \sigma_o e^{-\left(\frac{E_a}{kT}\right)} \qquad \ldots.(1)$$

where σ is conductivity, σ_o is the pre-exponential factor, E_a is the activation energy, k is Boltzmann's constant, and T is the temperature in Kelvin. By fitting the equation (1), a hopping-type conduction mechanism is confirmed with activation energy values of 96 and 59 meV for pristine and F-SnO_2 films, respectively, indicating a relatively facile charge transport process in the latter. Figures 7.6d and e show linear I-V characteristics for SnO_2 and F-SnO_2 films at 25 °C

and 150 °C, respectively indicating ohmic contacts across the film. At room temperature, the dark current is relatively higher for F-SnO_2 than that of pristine SnO_2 as expected from the resistivity measurements. An increase in the photocurrent by 2-3 orders was observed for both pristine and F-SnO_2 due to the increase in surface free electrons on UV-activated desorption of adsorbed oxygen and other gas molecules from the film surface [Morais et al., 2007]. At 150 °C, the dark current shows a similar trend of higher conductivity in F-SnO_2 in comparison to that of the pristine film. However, it is interesting to note that F-SnO_2 shows a relatively lower photoresponse compared to pristine SnO_2. The resistivity values have been calculated from the I-V curves for SnO_2 and F-SnO_2 and are summarized in Table 7.4.

Table 7.4: Resistivity change in SnO_2 and F-SnO_2 films with temperature and UV illumination.

	UV Conditions	Resistivity@87 K Ω.cm	Resistivity@298 K Ω.cm	Resistivity@423 K Ω.cm
SnO_2	dark	2656	13.62	6.99
	light	NA	0.07	0.26
F-SnO_2	dark	49	5.18	1.13
	light	NA	0.08	0.44

N.A: Not available

Figure 7.6f shows the relative conductivity changes in both the films due to contributions from thermal and photo-induced charge carriers. At higher temperatures, the expected increase in photo-induced conductivity in F-SnO_2 is compensated with an increased scattering of charge carriers; this effect is much less in the case of pristine films. Thus, a significant decrease in the resistivity, lesser sensitivity towards temperature, and higher charge transportation efficacy of F-SnO_2 make it suitable for optoelectronic applications, in general.

7.3.6 Sensor Integrated with Transparent Metal Mesh Heater

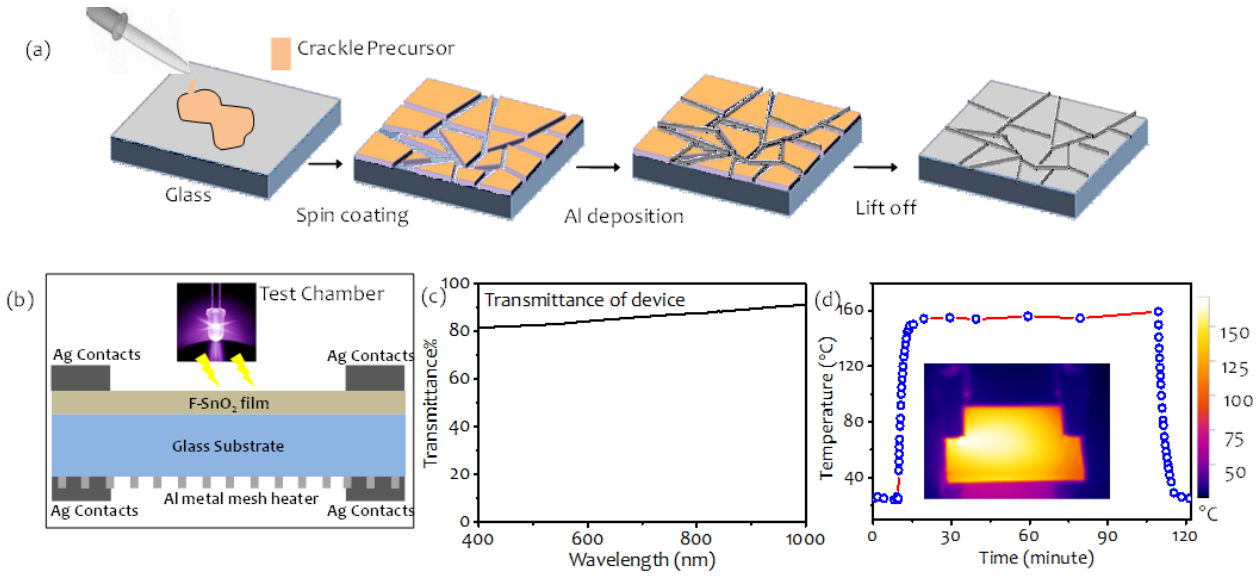

Figure 7.7: (a) Schematic showing the crack network templating process involved in the fabrication of Al-mesh network as transparent heater. (b) Sensor setup with integrated transparent metal mesh heater and UV-LED for temperature-dependent photoconductivity measurements. (c) Transmittance of SnO_2 film with integrated metal mesh heater. (d) Heating profile and thermal image of the metal mesh-based transparent heater at a temperature of 150 °C (operated at 6 V).

Using the crack network templating (done at Centre For Nano and Soft Matter Sciences, Bangalore) method as shown in Figure 7.7a, a transparent Al-mesh heater was fabricated on the other side of the glass substrate. In brief, when a thin film of an acrylic dispersion containing

suspension particles, such as a wet paint is applied on a nonporous surface, evaporation of the solvent concentrates the particles into a close packed array. Evaporation is accompanied by stresses in the wet film that deform the particles so as to close the pores. The film generally binds to the underlying substrate, generating shear stresses that resist deformation in the transverse plane and giving rise to transverse tensile stresses. When the magnitude of the tensile stress exceeds a critical value, cracks nucleate, thereby compromising the mechanical integrity of the film. The nature of crack network depends crucially on the uniformity of the layer thickness and also on the size, shape, and hardness of the colloidal particles. In this study, Al-mesh was deposited on the other side of the SnO_2 film for localized heating of the deposited films, as shown in Figure 7.7b and described in Experimental section in details. The total transmittance of the pristine or F-SnO_2 film combined with the metal mesh heater is observed to be >80% (Figure 7.7c). The desired temperature is obtained by joule heating of the network by applying an externally regulated voltage as detailed in the experimental section. The set temperature of 150 °C could be obtained instantly and locally within few seconds by joule heating the film at 6 V (Figure 7.7d). The thermal image of the F-SnO_2 film at 150 °C and the associated temperature profile are shown in the inset of Figure 7.7d.

7.3.7 F-SnO_2 Photoresponse: Persistent Photoconductivity

The temperature-dependent photoresponse curves of pristine and F-SnO_2 films towards UV exposure are shown in Figures 7.8a-c. In both instances, the film was kept exposed to UV till a saturated response was achieved within a maximum response time of ~2 min, following which UV was turned off, and the decay profile was recorded. The sensor is initially in a high resistance state due to the adsorption of oxygen molecules on the pristine and F-SnO_2 films due to the formation of a depletion layer. On UV exposure, there is a decrease in resistance with the exciton formation resulting in a steep rise in the response curve (Figures 7.8a-c). In this process, the photo-excited hole neutralizes the chemisorbed oxygen, and the electron is released to the conduction band thus reducing the depletion layer width and increasing the surface conductivity of pristine and F-SnO_2 film.

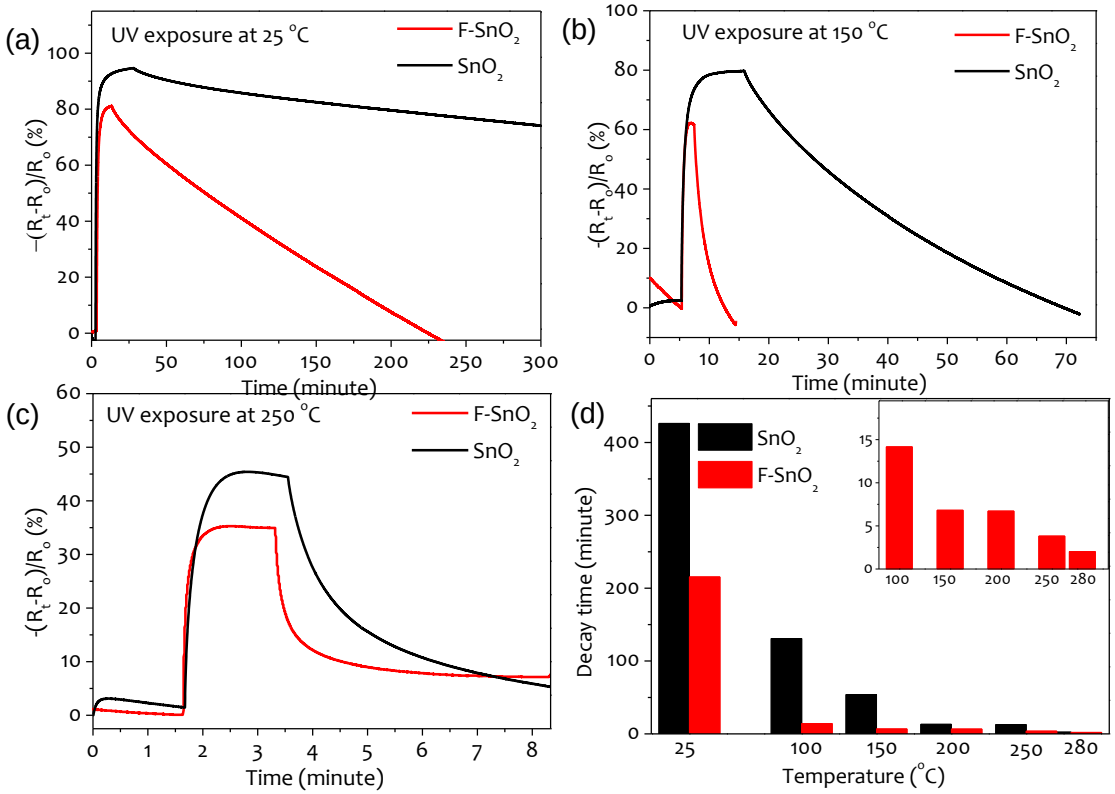

Figure 7.8: Photoresponse of SnO_2 and F-SnO_2 towards UV source of 365 nm wavelength at (a) 25 °C, (b) 150 °C, and (c) 250 °C. (d) Temperature dependence of photoresponse decay time.

A higher photoresponse in SnO_2 than in F-SnO_2 is understandable due to lesser number of active sites available for chemisorption of oxygen, post-fluorination. However, the sensitivity of F-SnO_2 is sufficient enough for obtaining a significantly measurable response. At room temperature, the response almost plateaus with a slow decay even after UV is turned-off. This effect of high photoresponse even after removal of incident light is well known as persistent photoconductivity that is observed in semiconductors [Geraldo et al., 2003; Liu et al., 2015a; Morais et al., 2007; Tierney et al., 2016; Viana et al., 2013]. Although, the decay time considerably reduces with an increase in temperature, it is interesting to note that F-SnO_2 film exhibits a much faster decay even at considerably lower temperatures (Figures 7.8b, c). At 150 °C, F-SnO_2 film exhibits a sharp decay profile with a decay time of ~ 7 min in contrast to the SnO_2 film (~ 54 min) due to enhanced scattering arising from an increase in density of free electrons. Further, as shown in Figure 7.8d, F-SnO_2 shows relatively lower decay times at all operating temperatures in the range, 25 - 280 °C.

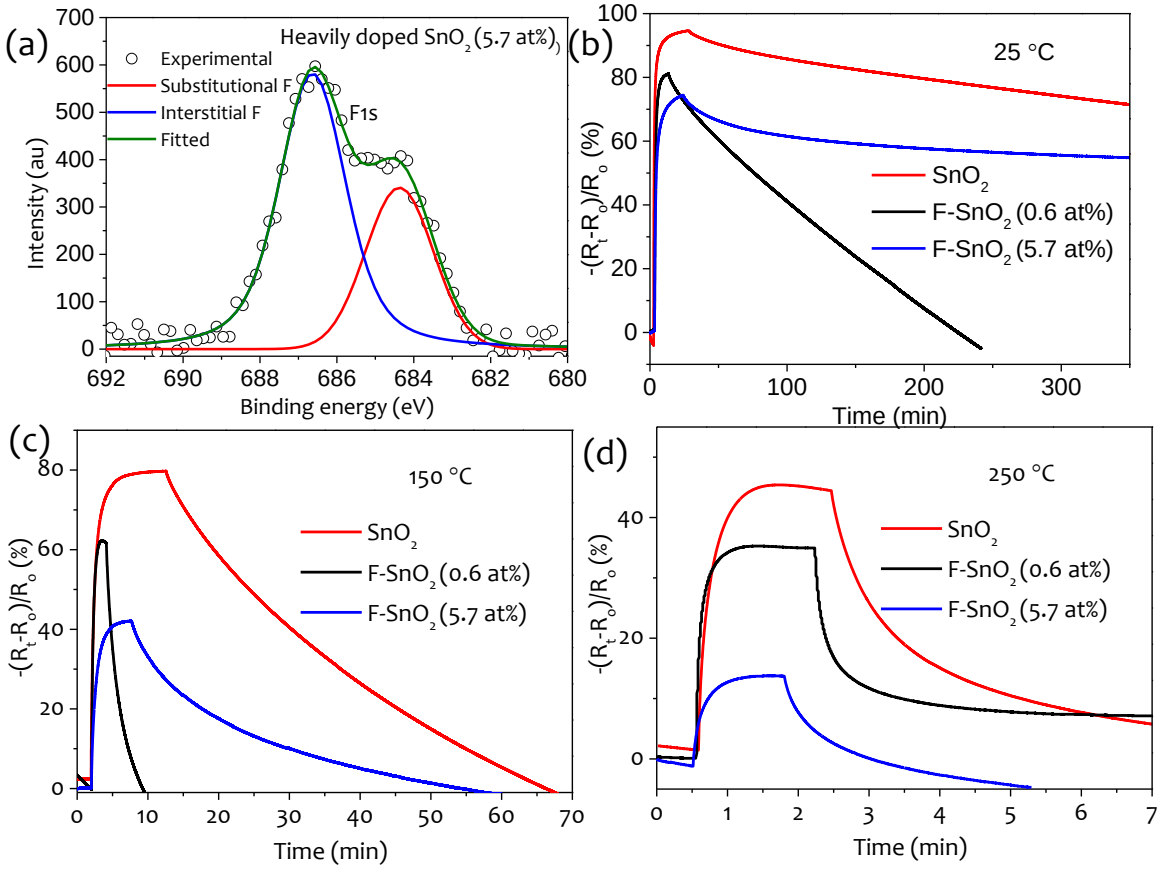

Figure 7.9: (a) High resolution deconvoluted F1s XPS spectra of heavily doped F-SnO_2. Photoresponse of SnO_2, lightly-doped F-SnO_2 (0.6 at%) and heavily-doped F-SnO_2 (5.7 at%) films towards UV-light at (b) 25 °C, (c) 150°C and (d) 250°C.

The same experiments were performed for a heavily-doped F-SnO_2 film (5.7 at%, doconvulated XPS spectra shown in Figure 7.9a). Surprisingly, the persistent photoconductivity became dominant for the heavily doped F-SnO_2 films with a much slower photo-decay profile (Figure 7.9b-d). Heavily doped F-SnO_2 exhibits a slow decay time ~33 min at 150 °C (Figure 7.9b). As observed in XPS analysis of heavily doped SnO_2 films, substitutional as well as interstitial doping takes place which can lead to a decrease in surface free electron due to internal compensations (Figure 7.9a) [Swallow et al., 2018]. It is probably due to this reason that fluorination of SnO_2 at high concentration does not lead to significant decrement in PPC.

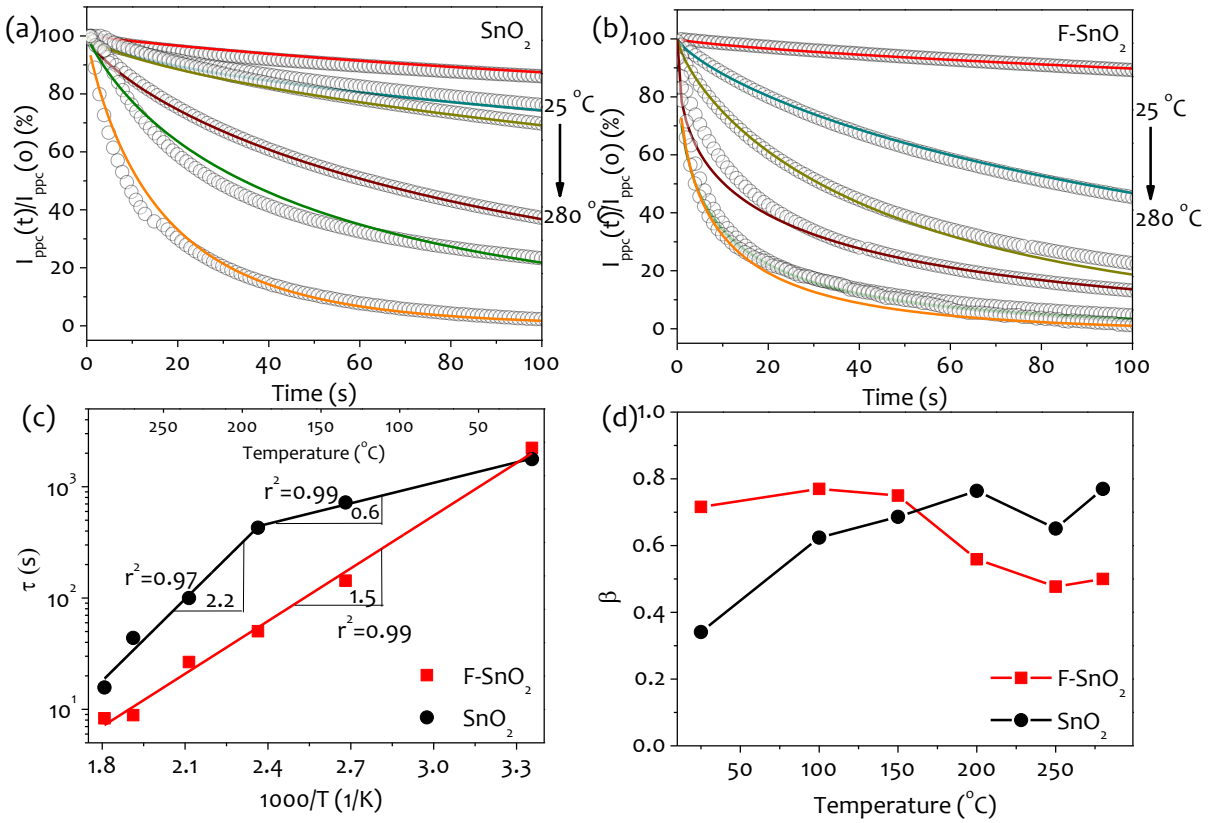

Figure 7.10: Normalized experimental data (open circle) overlaid with fitted (solid line) photocurrent decay curves at different temperatures for (a) SnO_2 and (b) F-SnO_2 films. Temperature dependence of (c) lifetime of photo-induced charge carrier (τ) and (d) decay exponent (β) for SnO_2 and F-SnO_2 films. Note: In Figure (c), data points are linearly fitted with the x-axis (bottom). The symbols are experimental data, and the connecting lines in (d) are only to guide the eye.

The decay profiles shown in Figure 7.10 were fitted with stretched-exponential function (equation 2) to understand the PPC behavior of pristine and F-SnO_2 films [Morais et al., 2007],

$$I_{PPC}(t) = I_{PPC}(0)e^{\left(-\frac{t}{\tau}\right)^{\beta}} \quad \ldots.(2)$$

where, $I_{PPC}(t)$ and $I_{PPC}(0)$ are induced photocurrents at time t and t=0 respectively, τ is the lifetime of photo-induced charge carrier, and β represents the decay exponent. From the fitted plots in Figure 7.10 (a and b), τ and β parameters were determined at different temperatures for both pristine and F-SnO_2 films. In Figure 7.10c, the pristine film shows two linear temperature-dependent regions. In the low operating-temperature range (25-150 °C), a slight decrease in τ with a slope of 0.6 is observed, later decreases sharply to ~ 2.2 in the range 150 °C to 280 °C (Figure 7.10c). On the other hand, the F-SnO_2 film shows a linear decrease in the entire temperature range (slope, 1.5), leading to approximately an order decrease in the τ value at 150 °C. Further, it possesses higher decay constant (β) of 0.71 at room temperature, which is not much influenced at high temperatures. This is due to the reduced surface potential barrier for O_2 adsorption even at room temperature because of increased scattering [Viana et al., 2013]. On the contrary; the SnO_2 film exhibits a lower decay constant, β of 0.34 at room temperature, which increases and saturates above 200 °C, compelling a high operating temperature in sensors (Figure 7.10d). Thus, the fluorination of SnO_2 films significantly enhances the photoconductivity decay upon turning-off the UV light illumination. Atom projected partial density of states (pDOS) of pristine, and F-SnO_2 (done in collaboration with Dr. S. Bhattacharya, Indian Institute of Technology, Delhi) reveals that the oxygen vacancies in SnO_2 are filled by F doping leading to an increment in conductivity, decrease in the persistent photoconductivity, and overall enhancement in photoconductive decay of the sensing device.

7.3.8 Response Towards Humidity

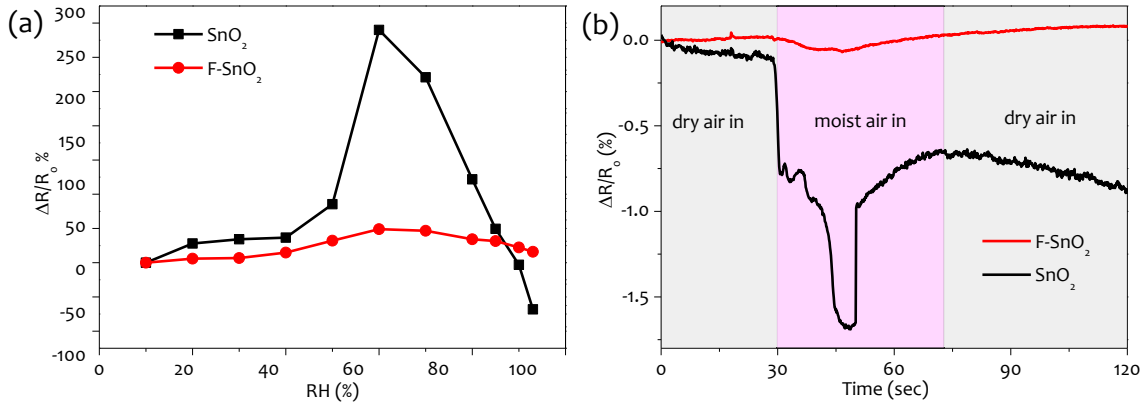

Figure 7.11: (a) The sensitivity of the pristine and F-SnO_2 films toward humidity at room temperature. (b) Change in resistances of the films under dry and moist air.

The sensing of volatile organics/gases from the environment or as a biomarker from human breath is always associated with the interference from the humidity in the enviromnet or in human breath. For this reason, the response of the fabricated sensor towards different relative humidity was analyzed. (Figure 7.11 a). It can be seen from the figure that F-SnO_2 film remain stable in the entire humidity range with insignificant response towards changing humidity. On the other hand, as expected, SnO_2 based device exhibit a significant response towards the changing relative humidty concentraions. The same has also been confirmed by changing the environment of the pristine and F-SnO_2 films from dry air to ambient air. As shown in Figure 7.11b, the resistance change is insignificant for F−SnO_2 in comparison to SnO_2 films.

7.3.9 Gas Sensing Characteristics

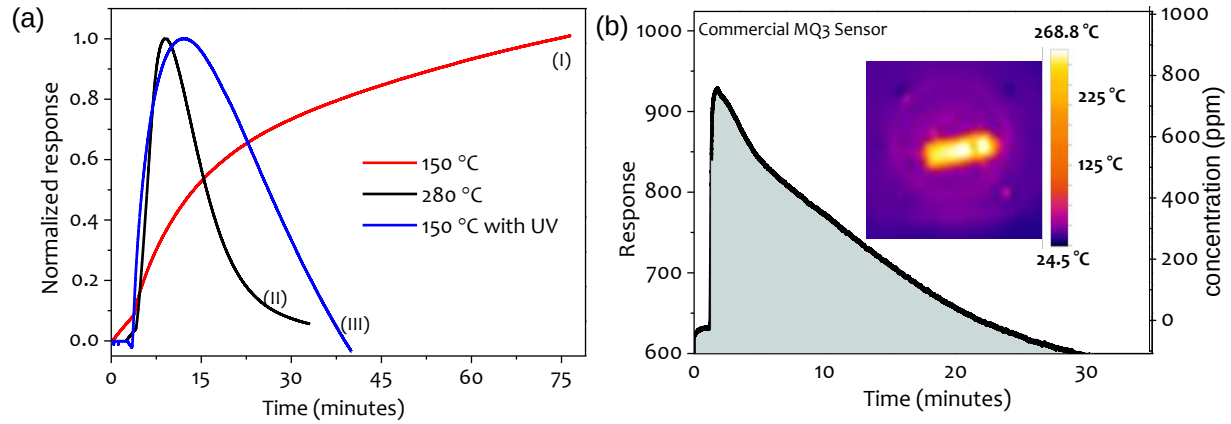

Figure 7.12: (a) Normalized response of F-SnO_2 sensor towards ethanol at different operating conditions. (b) Response of MQ3 sensor towards ethanol. Inset in (b) shows the thermal image of MQ3 sensor. The operating temperature of the sensor is ~260 °C.

The sensing setup used for the measurements is explained in the experimental section. The volatile organic vapors of fixed concentration with a non-steady state profile were created using a nitrogen gas flow for F-SnO_2 sensor testing. As shown in Figure 7.12a, the sensor, when operated at a lower temperature of 150 °C (red curve, I), on exposure to ethanol, attains a hangover-type state (device response plateau) that does not recover even when the ethanol concentration in the chamber is made zero. The ethanol vapors adsorb through the charged oxygen species as well as directly onto the sensor surface. These VOC molecules may or may not survive after they interact with adsorbed oxygen species. Some of the ethanol molecules react with $O_{2\,(ads)}^{-}$ type species adsorbed on SnO_2 surface to release free electrons along with CO_2, H_2O, etc. as gaseous by-products [Li et al., 2019]. However, at a moderate temperature of 150 °C, the reaction rate does not allow desorption of ethanol molecules to occur [Lin et al., 2019].

On the other hand, the sensor, when operated at high temperature (280°C), responds to ethanol and recovers gradually as ethanol concentration reduces (black curve, II), matching the response of a commercial MQ3 sensor (Figure 7.12b). The commercial MQ3 sensor is generally used for ethanol sensing in the range of 20-1000 ppm. The response of the MQ3 sensor is expressed as an integer value ranging between 0 to 1024. The linear response calibration curve of the commercial sensor is used for the estimation of ethanol concentration. MQ3 sensor is a SnO_2 based sensor that operates at an applied potential of 5 V. The MQ3 sensor is composed of a thick SnO_2 film deposited around the alumina ceramic tube with platinum electrode wires on top and a coiled Ni-Cr heating element inside the tube. The enveloped MQ-3 has six pins, four of them are used to fetch signals, and the other two are used for providing heating current. The operating temperature of the MQ3 sensor was measured to be 260 °C (inset, Figure 7.12b). It is clear that high operating temperature increases the adsorption of charged oxygen species (O^-, O^{2-}, or O_2^- type) on the sensor surface that act as ideal sites for VOC interaction and for faster desorption of chemisorbed VOCs [Lin et al., 2019]. Interestingly, the sensor response could be brought back to its baseline at 150 °C by complimenting with UV during exposure with ethanol vapors (blue curve, III). After UV exposure, the device current recovered to its baseline value due to the desorption of chemisorbed ethanol on the surface.

The current response of the sensor towards a lower steady-state concentration profile of 100 ppm of ethanol and triethylamine (TEA) is shown in Figure 7.13a and b respectively. The F-SnO_2 sensor responds to 100 ppm of ethanol in less than a minute and recovers back to its original state in 5 min after exposure.

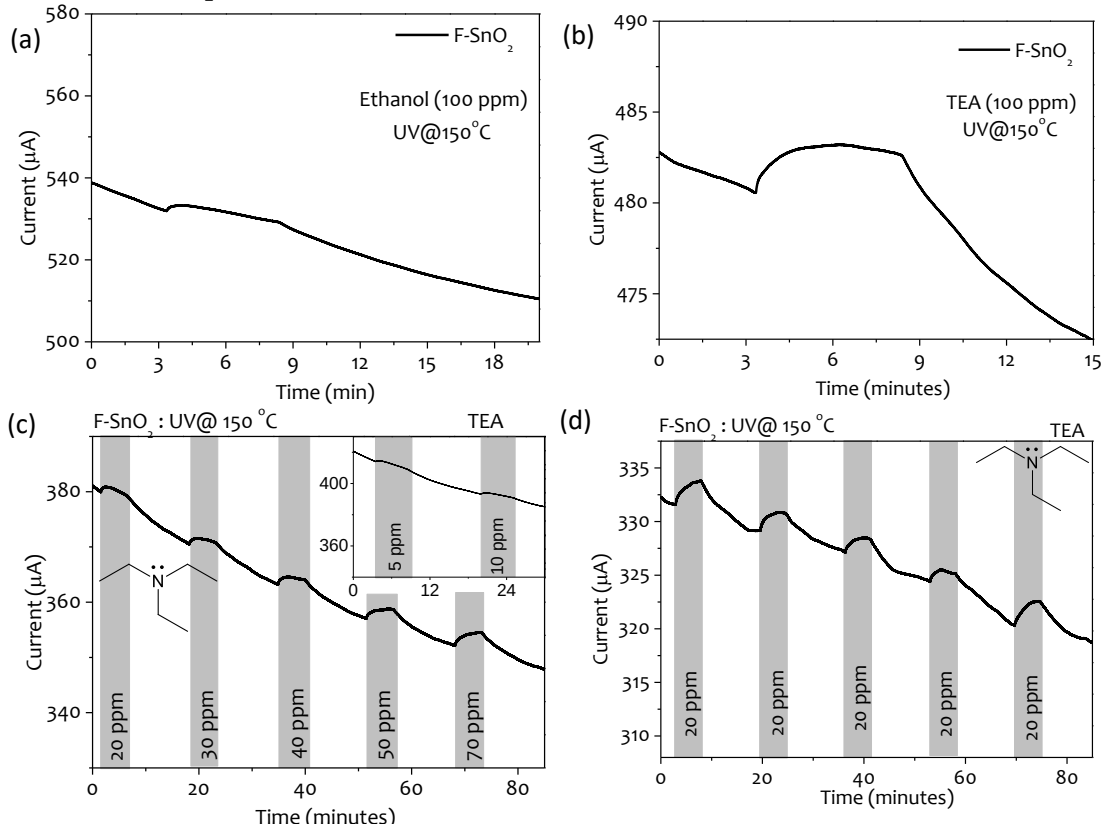

Figure 7.13: The F-SnO_2 sensing characteristics towards (a) 100 ppm of ethanol and (b) 100 ppm triethylamine (TEA) vapors. (c) Response of sensor towards different concentration of TEA (inset in c shows response at 10 and 5 ppm) and (d) same concentration (20 ppm) of TEA at 150 °C.

The sensor exhibited significant response even at low concentrations of TEA with a detection limit of 5 ppm (Figure 7.13c). Further, a stable and repeatable response towards repetitive exposure of TEA at 20 ppm can be observed (Figure 7.13d). However, the sensitivity of F-SnO_2 is expected to be lower in comparison to pristine SnO_2 due to reduced oxygen defects upon fluorination.

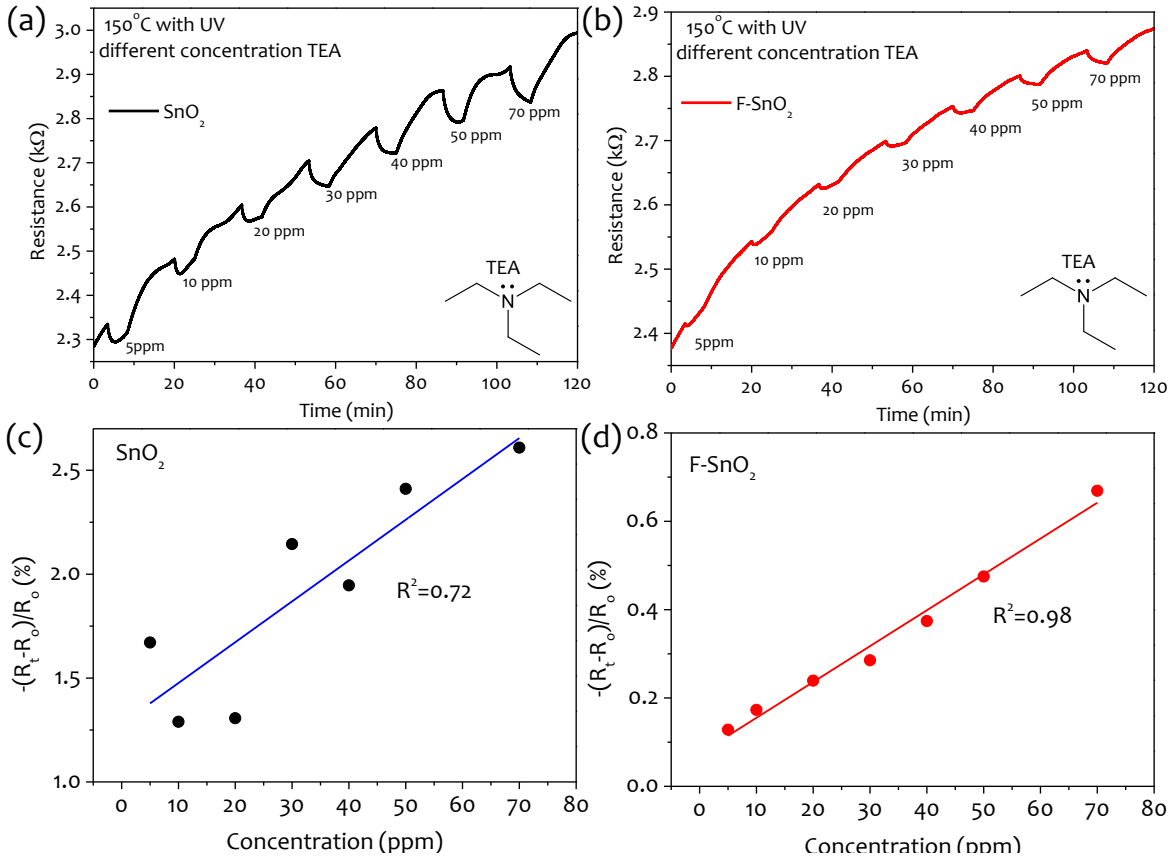

Figure 7.14: Sensing characteristics of (a) SnO_2 and (b) F-SnO_2 towards different concentrations of TEA vapors and (c,d) corresponding sensitivity profile with respect to concentration variation along with the R^2 values.

Despite higher sensitivity, SnO_2 based sensor is unreliable due to non-linear response with R^2 of 0.72 for low concentrations of TEA (Figure 7.14a and c). The instability in the SnO_2 based sensor can be due to the poisoning of the sensor at lower working temperatures (150 °C) despite the use of UV illumination [Korotcenkov et al., 2011]. Interestingly, F-SnO_2 based sensor shows an almost linear increase in sensitivity with concentration (R^2=0.98), exhibiting excellent sensor characteristics (Figure 7.14b and d). Fluorination of SnO_2 leads to a reduction in surface hydroxyls and oxygen defects, thus, inhibiting the detrimental poisoning effect, which is otherwise observed in pristine SnO_2.

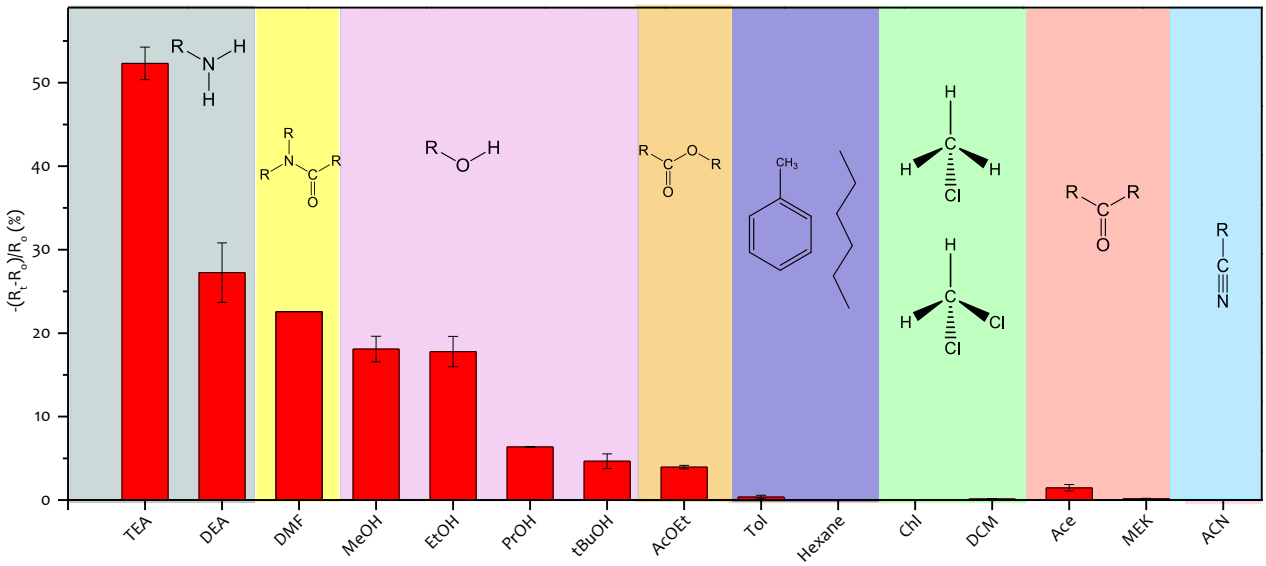

Figure 7.15: Histogram of F-SnO_2 sensor towards different target VOCs at 150 °C under UV-illumination. Note: The error bar is over three consecutive sensor measurements.

A variety of VOCs were exposed to the sensor as shown in Figure 7.15. It is observed that the relative response of the F-SnO_2 sensor towards VOCs of fixed concentration under similar conditions (150 °C with UV) is dominated by the electron-donating tendency of the functional group present (amines > amides > alcohols > ester > alkanes > halo-alkanes > carbonyl > cyanide). Amines with strong electron-donating effects produced the highest response, followed by amides, alcohols, and esters. The VOCs with no electron-donating tendency (carbonyls, alkanes, halo-alkanes, and cyano groups) had insignificant sensitivity with this sensor. Among alcohols, there is a reduction in sensitivity with increasing alkyl group (primary > secondary > tertiary) which could be attributed to the increase in steric hindrance, as reported in the literature [Hossein-Babaei et al., 2013]. The sensing mechanism can be explained on the basis of desorption of surface adsorbed oxygen by the VOCs, leading to an increase in electron density on the surface and thus decreasing the resistance of the sensor.

7.3.9 "Sensor-Reset" Process

Though the VOC sensor could be operated at 150 °C with UV, however, the practical applicability of the fabricated transparent display as a sensor is still a challenge with continuous illumination of the sensor even when not in use. Thus, a "sensor reset" mechanism relying on a reduced PPC effect (see schematic in Figure 7.2) using F-SnO_2 as sensor surface becomes imperative towards a transparent display-based VOC sensor (section 7.3.9). As seen in Figure 7.16, the sensor response saturates after exposure to ethanol and does not recover even when the VOC concentration gets to zero. At this stage, a UV pulse is fed till the generated photocurrent saturates, and as the UV is turned off, the sensor readily recovers to its original state. Hence, a photo-chemi-resistive sensor technology using fluorinated SnO_2 for efficient detection of VOCs is successfully demonstrated via an innovative "sensor reset" process.

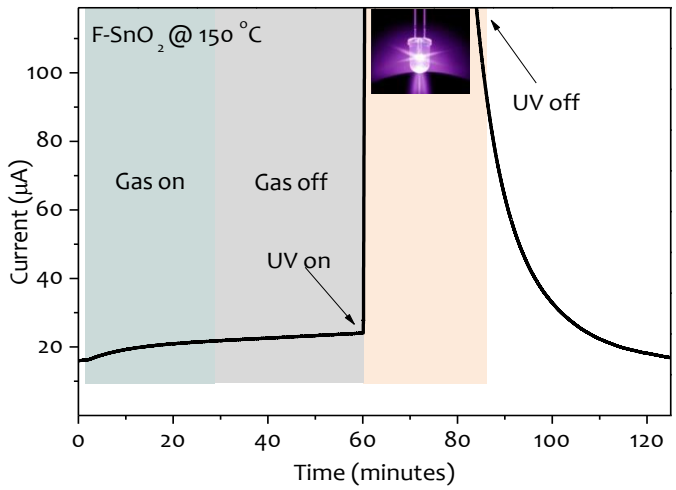

Figure 7.16: The sensor current response profile with the UV-on after saturated ethanol response is obtained at 150 °C. Note: Once the saturated photoresponse is obtained, UV is also turned-off for the complete recovery of the sensor.

7.4 Conclusions

In conclusion, a unique sensing concept-design is successfully demonstrated for VOC detection using fluorinated SnO_2 films. The fluorination of SnO_2 films (0.6 at.%) have been performed successfully using F-TEDA as the precursor. The extent of fluorination of SnO_2 could be readily optimized, keeping resistivity lower by an order magnitude without compromising the transmittance. The F-SnO_2 sensor showed a significant reduction in persistent photoconductivity at 150°C. The sensor exhibits a stable, ppm level response to different VOCs with relatively fast recovery in few minutes at 150 °C. Interestingly, the response is dominated by the electron-donating tendency with triethylamine showing the highest response amongst the analyzed VOCs. In addition, this work results in a UV-pulse based reset mechanism integrated to a

transparent display-based sensor since, in the case of sequential events, the VOC sensor in a ready-to-use form could be an urgent necessity. It can be used as a wearable item or even serve as a window panel in indoors where the VOC levels are often unregulated and pose a major health concern.